BAMS Article

Atmospheric and Insect Responses to a Total Solar Eclipse

Joshua Wurman,[a] Karen Kosiba,[a] and Paul Robinson[a]

KEYWORDS:
Ecology;
Boundary layer;
Ecosystem effects;
Radars/Radar observations;
Animal studies;
Biosphere-atmosphere interaction

ABSTRACT: How do the atmosphere and airborne insects respond to the abrupt cessation and restoration of sunlight during a total eclipse? The Flexible Array of Radars and Mesonets (FARM), including three mobile Doppler on Wheels (DOW) radars, mobile mesonets, Pod weather stations, and an upper-air sounding system, was deployed as an unprecedentedly dense observing network in the path of totality of the 21 August 2017 eclipse that spanned the United States from its Pacific to Atlantic coasts. This was the first targeted dual-polarization radar, multiple-Doppler, and micronet study of the impacts of totality on meteorology and insect behavior. The study area was chosen to be completely sunny, nearly devoid of trees, with homogeneous, nonforested land use, and very flat. This resulted in as near an ideal observational environment as realistically attainable to observe the effects of a total solar eclipse absent the confounding effects of variable cloud shading, terrain, and land use. Rapid and substantial changes in the boundary layer and propagation of a prominent radar fine line associated with a posttotality wind shift mechanism different than previously hypothesized were observed. Profound and rapid changes in airborne insect behavior were documented, including descent and then reascent during the minutes immediately surrounding totality, with implications related to solar-related insect navigational mechanisms and behavior.

SIGNIFICANCE STATEMENT: We document, for the first time, the fine-temporal and spatial-scale evolution of the atmosphere, and detail, for the first time, the rapid response of insects to complete totality during a solar eclipse. Targeted high-spatiotemporal-frequency observations during totality across a small observational domain, chosen specifically for clear skies, flat terrain, and nonforested land use, permit the first fine-scale quantification of kinematic/entomological responses to totality nearly absent confounding nonsolar factors. A posttotality radar fine line causing a wind shift is observed. Insect behavior during totality is qualitatively different than during near-, even 98%-, totality, with cross-disciplinary implications related to insect navigation and migratory behavior.

DOI: 10.1175/BAMS-D-24-0165.1
Corresponding author: Wurman, jwurman@cswr.org
Supplemental information related to this paper is available at the Journals Online website: https://doi.org/10.1175/BAMS-D-24-0165.s1.

Manuscript received 9 June 2024, in final form 17 February 2025, accepted 22 March 2025

AFFILIATION: [a] Flexible Array of Radars and Mesonets, The University of Alabama, Huntsville, Alabama

1. Introduction

That solar eclipses affect the atmosphere has been known since antiquity. But, detailed quantitative observations only exist much more recently. A review of observations of atmospheric changes associated with 44 different eclipses dating back to 1834 is provided in Aplin et al. (2016). Gray and Harrison (2016) document changes in boundary layer winds by analyzing a dense network of observing stations impacted by an eclipse crossing the United Kingdom in 2015. The effects of eclipses on observed weather radar reflectivity, inferred changes in the atmospheric boundary layer (ABL), and the inference of heat fluxes from radar data are documented in Rabin and Doviak (1989).

A solar eclipse is described as "an experiment by Nature. . . eliminating the influence of other known phenomena" (Clayton 1901). However, the quantification of the effects of any eclipse is usually confounded by a conflation of nonsolar effects including spatially and temporally heterogeneous cloud cover, varied terrain and land use, evolution of ambient meteorological fields independent of the eclipse, and spatial gradients in the decreases in solar insolation across broad swaths of eclipse totality and nontotality. Radar observations of the ABL in the path of totality are rare and typically of coarse resolution. For example, observations such as those in Rabin and Doviak (1989), using annuli bounded by 30–50-km range, were not able to characterize the ABL in the lowest 1 km above ground level (AGL). The extensively studied 2015 British Islands eclipse crossed hilly terrain with a great variety of wooded, agricultural, residential, industrial, and other urban and rural characteristics.

Pedants sometimes note that nearly every meteorological "experiment" is not truly an experiment, but rather an "observational study." In this reasoning, experiments feature randomization, replication, and controls (e.g., Shaffer and Johnson 2008), qualities nearly impossible to achieve in observational studies of large-scale (larger than a laboratory or wind tunnel) atmospheric phenomena. Every snowflake, tornado, extratropical cyclone, and ABL region differs from all others for myriad uncontrollable and unrepeatable reasons. Lacking the ability to control for critical influential variables, observational scientists collect statistics and produce climatologies, spanning a hopefully representative sampling of phenomena ranging from cyclones (e.g., Sanders and Gyakum 1980) to tornadoes (e.g., Wurman et al. 2021a) to nonmeteorological phenomena as diverse as carcinogenesis (e.g., Armitage and Doll 1954), or produce analyses based on large numbers of essentially uncontrolled observations (e.g., Gray and Harrison 2016). Since total solar eclipses are comparatively rare (compared to tornadoes, hurricanes, extratropical cyclones, or carcinogenesis), this type of climatological/statistical analysis of eclipse effects is not practical.

2. Targeting the eclipse

The 21 August 2017 North American total solar eclipse provided a rare opportunity to conduct an observational study more closely approximating a controlled experiment than is typically possible. The precise path, timing, and characteristics of eclipses can be predicted decades, even centuries, in advance (e.g., NASA 2024). It was known that the path of totality across the United States (Fig. 1) would cross regions with varying topographic and land-use

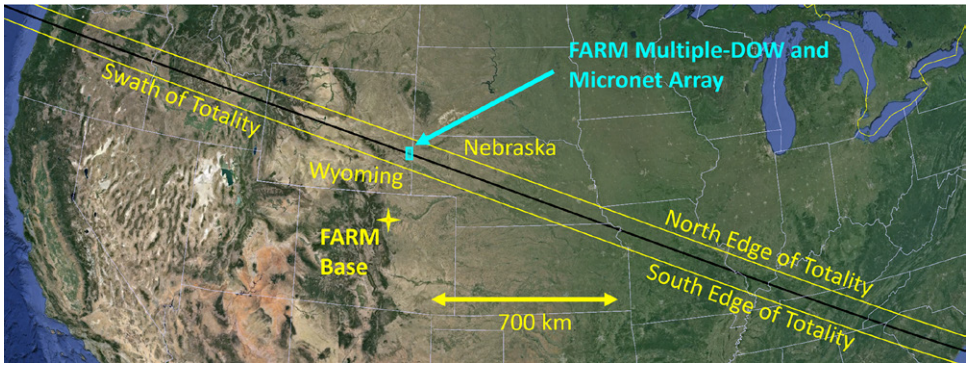

Fig. 1. Path of eclipse and FARM multiple-DOW/micronet array. Path of the 2017 eclipse across North America, totality edges in yellow and the center in black. A small rectangle approximately delineates the study region shown in Fig. 3.

characteristics. Three mobile Doppler on Wheels (DOW) radars, three mobile mesonets, twelve 1 m AGL Pod weather stations, and a mobile upper-air sounding system from the Flexible Array of Radars and Mesonets (FARM) (Wurman et al. 2021b) were available for this study. Since the DOWs and associated mobile mesonets, Pods, and mobile sounding systems were mobile and quickly deployable and well suited for targeted fine-scale observations of a variety of phenomena ranging from tornadoes (e.g., Wurman et al. 1996, 2012; Wurman and Kosiba 2013; Kosiba et al. 2013, 2024), hurricanes (e.g., Wurman and Winslow 1998; Kosiba and Wurman 2014; Wurman and Kosiba 2018), wildfires (Wurman and Weygandt 2003), to winter/alpine precipitation (e.g., French et al. 2018; Steiger et al. 2013; Kosiba et al. 2019), and, most germainly, ABL structure and evolution (e.g., Weckwerth et al. 1999, 2004; Marquis et al. 2007; Geerts et al. 2017; Rappin et al. 2021; Lachenmeier et al. 2024), it was possible to choose several potential regions in which to establish an ultrafine-scale targeted observational array with rare certainty that the phenomenon would occur when and where predicted.

It was critical to choose an observational domain very likely to be free of clouds and atmospheric boundaries during the periods leading up to, during, and after the eclipse, and this was, of course, not possible to predict well in advance. One to two days before the eclipse, a broad region extending through Wyoming and Nebraska was forecast to be relatively clear. To simplify data interpretation and analysis, it was desirable to choose a domain characterized by minimal terrain and land-use variation. This excluded much of mountainous and forested Wyoming and portions of Nebraska in the Platte River valley and Sand Hills. In addition, it was considered desirable to deploy a dense array of instrumentation near the center of the path of totality to minimize the effects of advective contamination from the fringe areas of totality. One day before the eclipse, a site survey team chose two domains each comprising several well-suited DOW and Pod sites in the center of the path of totality in very flat, nearly tree-free, sparsely populated regions of far western Nebraska and eastern Wyoming. The night before the eclipse, DOWs, other instrumentation, and crew traveled from the FARM base in Boulder, Colorado, to eastern Wyoming, within easy driving range of the potential domains. Short-lead-time forecasts, satellite observations, and surface analyses during the morning of the eclipse suggested that high thin clouds might impact western Nebraska, so the eastern Wyoming domain was chosen. The study region was too distant from National Weather Service surveillance radars, and the spacing of meteorological observing stations in this sparsely populated region precluded the resolution of any small, or especially subtle, preexisting boundaries, so their presence cannot be firmly excluded. However, surface analyses and satellite observations indicated that the study region was likely free of significant cloudiness and atmospheric boundaries (Fig. 2).

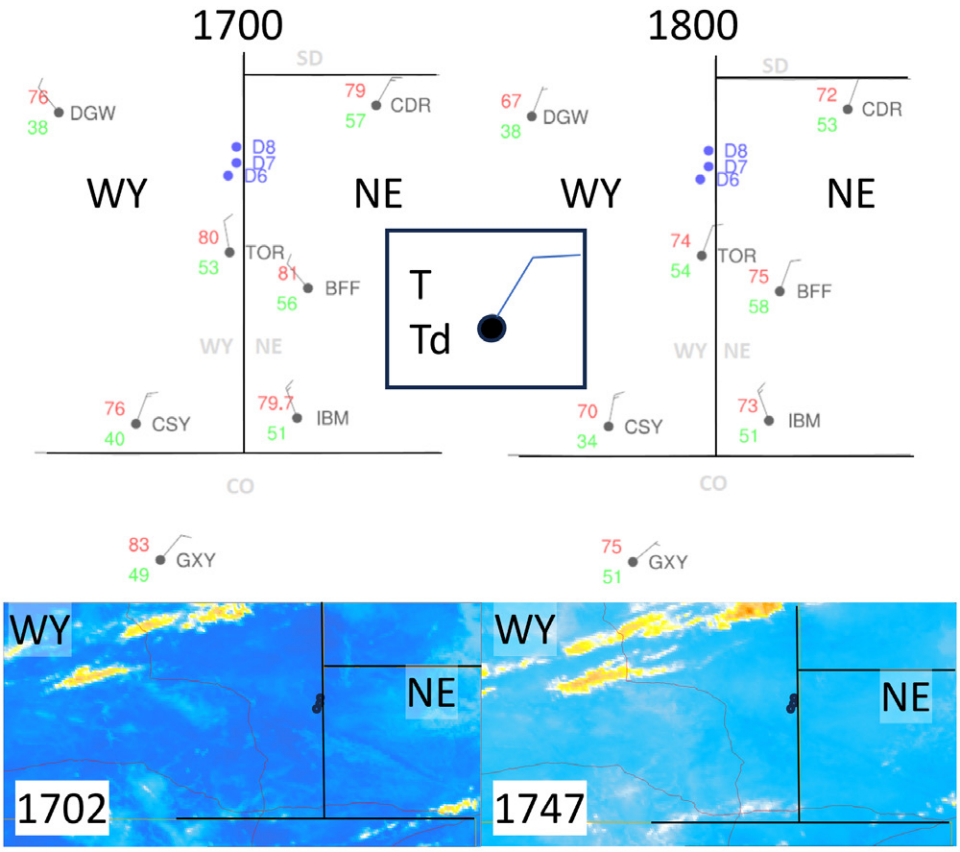

Fig. 2. Surface weather and cloudiness before and during the eclipse. (top) Surface weather station observations [*T*/*Td* is temperature/dewpoint temperature in °F, full wind barbs 10 kt (1 kt ≈ 0.51 m s^{-1}), half 5 kt] illustrating generally warm and dry conditions with light northerly winds over the candidate deployment areas and the final radar array. No obvious fronts or boundaries are evident. (bottom) The Geostationary Operational Environmental Satellite–R Series (GOES-R) longwave satellite depiction of cloudiness illustrating very clear skies (blue indicates a view of warm ground) before and during the eclipse, with cooler returns from clouds (white/yellow/orange). DOW locations are indicated in all panels along with state boundaries. Times are in HHMM UTC.

Targeted studies of the atmospheric-only responses to the 2017 eclipse as it crossed the complex terrain and land-use regimes in the southeastern United States were conducted using a fixed mesonet and deployable profilers [Mahmood et al. 2020 (hereafter M20)] and a deployable unmanned aerial system (UAS) (Buban et al. 2019). Using data from the widely spaced and fixed Kentucky Mesonet and from mobile profiling systems spaced 20–30 km in the path of totality during the eclipse, M20 documented a temperature decrease of about 4°C and a decrease in wind speed of up to 2 m s^{-1}, with the wind speed minimum occurring about 2400 s after totality. Vertically pointing LiDAR observations revealed relatively steady return intensity below 1.3 km AGL, but a substantial reduction in turbulent motions ~1000 s before totality. Turbulent motions developed again ~1000 s after the eclipse dropped below 50% obscuration. The 915-MHz profiler observations revealed a rapid decrease, then increase, of returned signals in the BL, with a simultaneous decrease in inferred turbulence. Notably, observations were absent, or of poor quality, below 200 m AGL (LiDAR) and 300–400 m AGL (915-MHz profiler). In Tennessee, Buban et al. (2019) used a combination of UAS and surface data during the eclipse to document significant atmospheric cooling below 50 m AGL, with a drop of about 5°C at 1.5 m AGL at 780 s after peak totality. Studies of the impacts of the eclipse on animal flight, primarily outside totality, were conducted by Nilsson et al. (2018) and Stepanian and Wainwright (2020).

3. Ultrafine-scale eclipse observational array

Three DOWs were deployed in a very open, flat, undeveloped area nearly devoid of trees, in an approximately north–south line with baselines of 8.7–9 km (Fig. 3). A dense micronet array of quickly deployable weather station Pods was placed in a north–south line 3–8 km west of the DOWs, paralleling the DOW line, with an interPod spacing of approximately 1 km, within a dual-Doppler lobe, and well within the region experiencing totality. Pods and DOWs were deployed well away from sparsely spaced buildings and trees, and away from small dips/valleys in the terrain, where possible. Pods, mobile mesonet pick-up trucks, and a DOW-mast-mounted weather station at 18 m AGL measured winds, temperature, relative humidity, and pressure (Fig. 4). The sounding system executed launches during the eclipse from near DOW6. The DOWs conducted rapid-update volumetric surveillance scans of the ABL, with 50-m range gating and 50-s volumetric updates, measuring fields of radar reflectivity, differential reflectivity (ZDR), Doppler velocity, and other parameters to map ABL structures including horizontal convective rolls (HCR; e.g., Weckwerth et al. 1997), and insects (e.g., Wilson et al. 1994; Geerts and Miao 2005a,b,c; Zhang et al. 2006; Stepanian et al. 2016). Details concerning instrumentation specifications and analysis methods are provided in the appendix. Totality in the study area lasted 168 s, centered just before 1748 UTC (all times hereafter in UTC), and skies remained nearly clear over the study area.

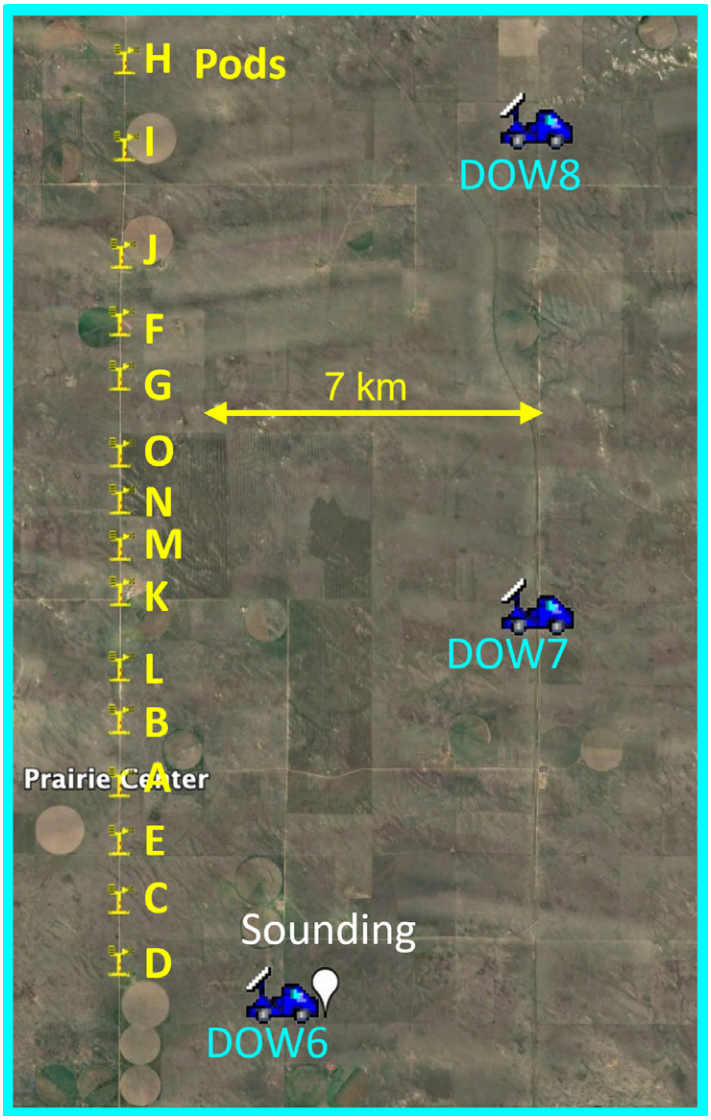

FIG. 3. FARM DOW/targeted micronet. Three DOWs (blue), 12 Pods (yellow), and a mobile sounding system (white balloon).

This was the first targeted radar, sounding, and micronet deployment in a total eclipse, including the first integrated multiple-Doppler dual-polarization network targeting totality. It was thus capable of revealing qualitatively improved, finer spatiotemporal scale, three-dimensional ABL and insect impacts compared to previous studies (e.g., Aplin et al. 2016; Gray and Harrison 2016; Rabin and Doviak 1989; Clayton 1901; Hanna et al. 2016; Clark 2016), and coarser targeted and nontargeted studies of this same eclipse (e.g., M20; Buban et al. 2019; Nilsson et al. 2018; Stepanian and Wainwright 2020).



Fig. 4. FARM DOW and micronet instruments. (left) Pod E deployed in an open area before totality; (center) DOW scanning during totality, with the sun at the time of totality visible at the top right; and (right) balloon sounding being launched before totality.

4. Atmospheric and insect responses

a. In situ measurements of thermodynamic and kinematic responses. As expected, the reduction in solar insolation during the eclipse resulted in changes in the structure of the BL, resulting in a decrease of near-surface temperatures (Fig. 5). One meter AGL Pod temperatures decreased 4°–5°C, reaching minima at about 1759 UTC, ~700 s after totality, while 18 m AGL DOW mast temperatures dropped nearly 3°C, reaching minima at about 1809 UTC, ~1300 s after totality. These drops were substantially larger than the mean 0.91° and 1.02°C drops noted in clear-sky weather stations during the total eclipse observed in Hanna et al. (2016) and Clark (2016), respectively, even though there was >87% obscuration at all the stations in these other studies but were similar to the 5°C drop at 1.5 m AGL reported by Buban et al. (2019) and the 4.5°C drop reported by M20. The magnitude of the average temperature decrease/recovery rates (dT/dt) exhibits complex behavior. Cooling rates are typically –0.001°C s^{-1} (3°C h^{-1}) during 1647–1730 UTC, with cooling intensifying sharply to 0.002°–0.003°C s^{-1} (7°–10°C h^{-1}) during 1744–1752 UTC, during and immediately surrounding totality when solar obscuration exceeded 95%. The posttotality recovery rate increases from 0 to +0.002°C s^{-1} by 1817 UTC and then averages +0.0015°C s^{-1} from 1822 to 1847 UTC as obscuration dropped to about 40%, with temperatures exceeding pre-eclipse values by about 1850 UTC, 3600 s after totality, when obscuration had dropped below 20%. (Individual station temperatures exhibited shorter-period oscillatory behavior, discussed below.)

These cooling and recovery rates are somewhat larger than the 1°C $(15\ min)^{-1}$ (0.0011°C s^{-1}) reported by M20. Lag times between totality and temperature minima were consistent with Hanna et al. (2016), M20, and Buban et al. (2019). Slightly larger temperature responses were measured at Pods deployed in very small minima in elevation (very shallow "valleys," with amplitudes of up to ~5 m). The causes of the temperature decreases and recovery are complex, since the effects of decreasing incoming shortwave radiation are initially affected by the evolution of dry-convective plumes in the BL; then these plumes (and associated HCR structures) weaken and/or elevate away from the surface layer, but residual effects may persist and be associated with oscillations (see discussion of temperature and wind speed oscillations below). These processes likely affect the accelerating rate of decay and subsequent more

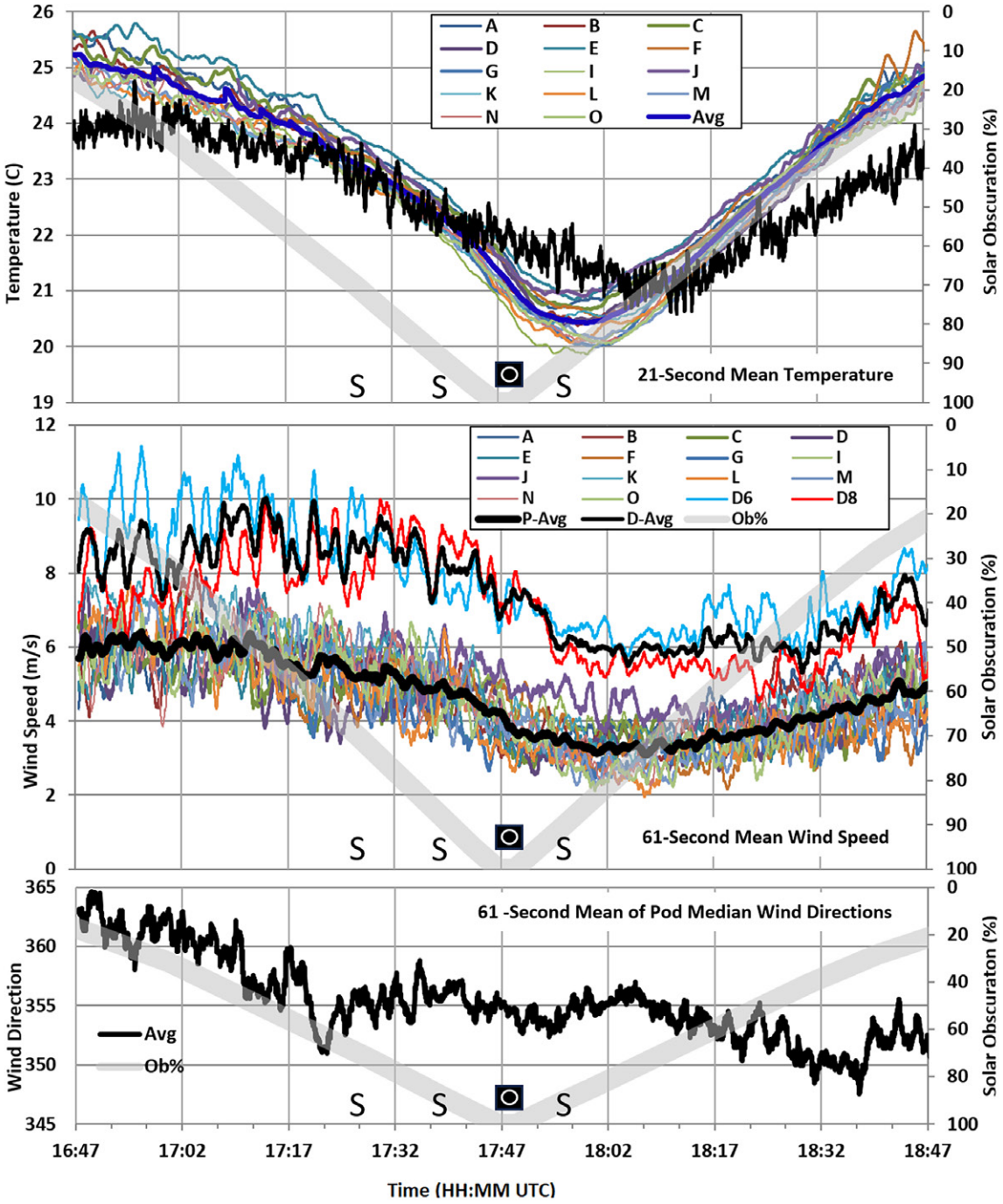

Fig. 5. In situ near-ground thermodynamic observations. Evolution of near-surface temperature and winds in the ABL during the eclipse as measured by Pods and DOW masts. (top) Temperature, (middle) wind speed, and (bottom) wind direction (degrees clockwise from north). Solar obscuration percentage is illustrated with thick gray lines. In this figure and others, the black circle and square icons highlight the time of totality. Sounding launch times are indicated with "S" in each panel.

linear recovery. [The detailed processes of ABL evolution, detailed responses of the ABL to changes in insolation, the effects of surface transpiration, and other effects are well covered in texts such as Stull (1988) and elsewhere and are beyond the scope of this manuscript.]

One-meter AGL wind speeds dropped from about 6 m s^{-1} before totality to about 3 m s^{-1} about 900 s after totality, while 18 m AGL winds dropped from about 9 to 6 m s^{-1}, with a very broad minimum from 500 to 2500 s after totality (Fig. 5), consistent with the observed increased near-surface stability (discussed below). The magnitudes of the wind speed changes were larger than reported by M20, but the fractional change was less. At both 1 m AGL and

18 m AGL, the minima in wind speeds trailed the minima in temperature. The minima in wind speeds at 1 m AGL trailed totality by about 900 s, substantially less than the 2400-s lag reported by M20, but the 18-m wind speed lag was less, but not as inconsistent with M20. Wind speed recovery at both 1 m AGL and 18 m AGL was slow and incomplete, with speeds ~1 m s^{-1} lower than pretotality values >3500 s after totality. This is somewhat different from the full recovery noted in a single station by M20.

One-meter AGL wind direction was nearly constant during the period from –1700 to + 1000 s from totality, with insignificant mostly monotonic variation, backing from 362° (2° east of north) 3600 s before 100% totality to 355° at totality and then backing to 349° 2900 s after totality, with an average backing rate of 0.002° s^{-1}, recovering to 352° at 3600 s after totality, all within 355° ± 7° (Fig. 5). It is difficult to compare these results with those of M20 since their Fig. 4 (Warren site) illustrates strong veering well prior to totality and then strong backing beginning just prior to totality, but their text describes strong veering during totality, and also backing followed by veering in their summary. It is possible that the quasi-steady wind direction, ~355° from about 1722–1805 (±~1600 s from totality) was due to a superposition of a slight, <4°, veering onto the slow secular background backing during the greatest solar obscuration. (A much later change in radar-observed direction associated with a singular radar-observed fine line is discussed below.)

Time histories of individual observing stations (Fig. 6) reveal quasi-periodic oscillations in wind speeds. FFT analyses (not shown) reveal peak energy in periods of ~300 s. It is notable that an ~300-s periodicity is roughly consistent with 1–1.5-km-scale convective structures (see discussion of radar-observed structures below), propagating across individual stations at about the observed wind speeds of ~5 m s^{-1} (~1500 m/~5 m s^{-1} = ~300 s). Oscillations continue through totality, suggesting that BL convective processes persist until totality. The oscillation amplitude decreases by >50%, from ~2 to <1 m s^{-1}, comparing 1647–1742 UTC to 1742–1807 UTC and then recovers to ~1 m s^{-1} after 1807 UTC. This suggests that residual convective structures persist, but weaken, in the eclipse-affected ABL during the period from 350 s before to 1100 s after totality, somewhat inconsistent with what is reported in M20, with the important caveat that their LiDAR (915-MHz profiler) data did not extend robustly below 200 (300–400) m AGL. (Details concerning manifestations of BL convective processes are beyond the scope of this work.) Time histories of temperature change (dT/dt) reveal an apparently noisier (due to quantization of temperature measurements compared to very small second-to-second temperature changes) but similarly oscillatory behavior, with FFTs also revealing ~300-s periodicity. The amplitude of the oscillations was substantially reduced during 1720–1827 UTC, a much longer suppressed period compared to the wind speed history. The correlation between dT/dt and wind speed at Pods M, N, and O was moderate, ranging from +0.4 to +0.6.

An abrupt clockwise wind shift of ~50°, a reduction in speed of ~3 m s^{-1}, and an increase in dewpoint of ~5°C associated with the passage of a radar fine line (discussed below) were observed by the DOW mast and some Pods from 1940 to 1950 (well after the eclipse period illustrated in Figs. 5 and 6, and after Pod retrieval had commenced and radar operations had ceased), well after eclipse "last contact" at 1913 and the end of solar obscuration. This wind shift is distinct from, and well separated in time from, the during-eclipse wind speed and direction evolution analyzed here.

Atmospheric balloon soundings (Fig. 7) were launched before totality at 1727 and 1739 UTC and after totality at 1755 UTC. Soundings ascended at ~4–5 m s^{-1}, reaching 1 km AGL 198–270 s after launch, and reaching 100 m s^{-1} ~20 s after launch. Wind speeds increased from 8 to 9 m s^{-1} from just west of north (346°–356° measured clockwise from north) near the surface to ~10.5 m s^{-1} from the north (360°–367°) at 700 m AGL at all the sounding times. There was no substantial change in ABL wind speeds or directions above 100 m AGL during

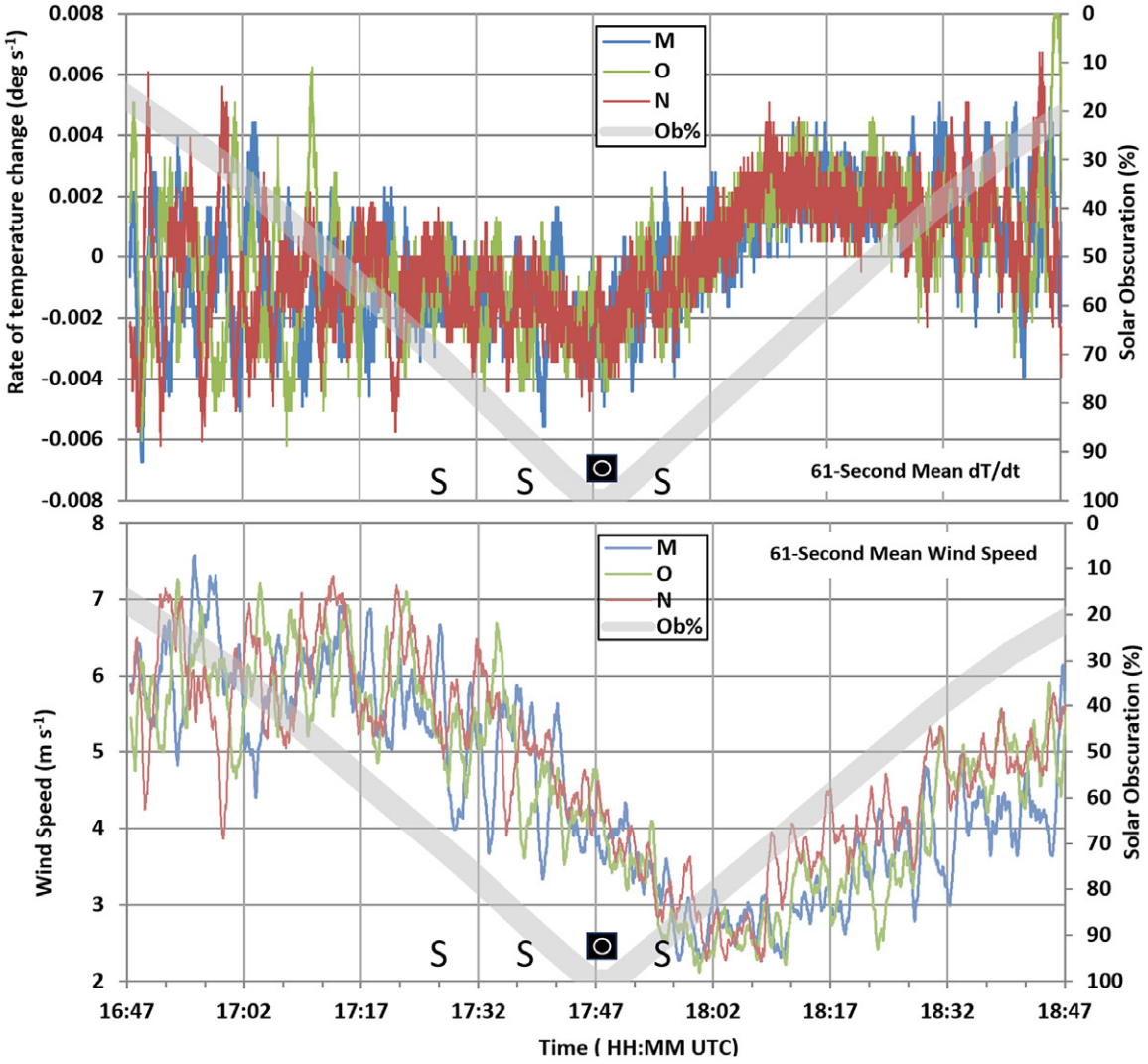

Fig. 6. In situ near-ground thermodynamic observations from selected Pods. Evolution of 1-m temperature changes and wind speed oscillations in the ABL during the eclipse as measured at Pods M, N, and O. Solar obscuration percentage is illustrated with thick gray lines. (top) *dT/dt* and (bottom) wind speed. Sounding launch times are indicated with S in each panel.

the eclipse. From 100 to 700 m AGL, wind speeds vary only slightly from 1727 to 1755 UTC. Maximum decreases of <1 m s^{-1} occurring ~300 m AGL and ~1.5 m s^{-1} occurring near the top of the boundary layer, in contrast to the very near-surface Pod (1 m AGL) and DOW mast (18 m AGL) data, demonstrate that the ABL bulk wind response was restricted to very near the surface.

Potential temperature profiles before and after totality reveal a roughly neutrally stable layer of ~700-m depth before and ~900 m after, totality. Prior to totality (1727 and 1739 UTC), ABL potential temperatures above 100 m AGL increased very slightly by about 0.1°C, then dropped by about 0.3°C by 1755 UTC, consistent with initial residual dry convective circulations upwardly transporting buoyant parcels, followed by slight cooling in the absence of incoming solar radiation. Potential temperature profiles are roughly either statically neutral or stable in the ~100–750-m layer and the ~100–950-m layer before and after totality, respectively. A statically unstable surface layer in the lowest ~40 m at 1727 UTC (roughly 70% obscuration, see Fig. 5) is subsequently eliminated and replaced by a strongly statically stable layer in the lowest ~100 m by 1739 and 1755 UTC (> 90% obscuration, see Fig. 5). The deepening of the ABL was consistent with the presence of residual dry convective updraft motions.

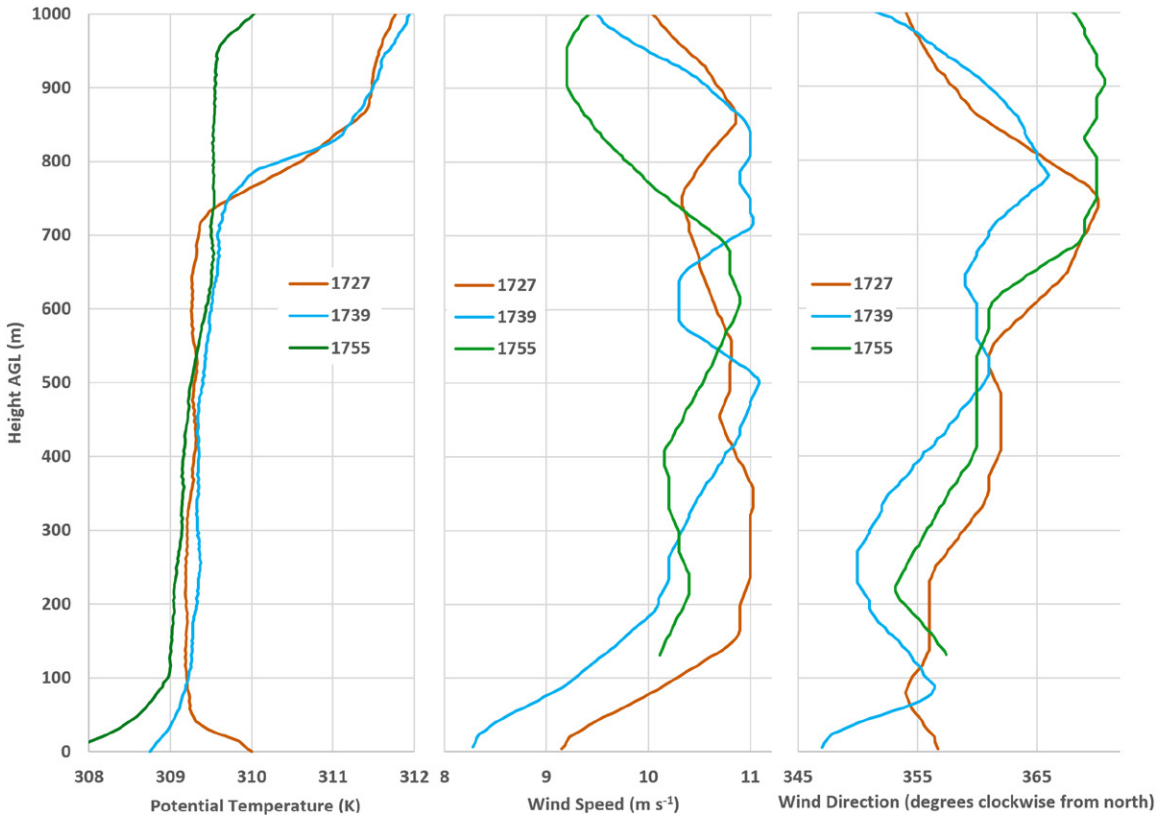

Fig. 7. Balloon Soundings during the eclipse. (left) Potential temperature, (center) wind speed, and (right) wind direction. Sounding launch times are in HHMM UTC.

More substantial potential temperature drops observed by the soundings from 40 to 100 m AGL are consistent with stabilization of the layer immediately adjacent to the ground as a result of the loss of sensible heating and vertical mixing [reported sounding temperatures below 40 m AGL are a blend of surface initialization and measured temperatures, illustrating that much of the cooling occurs below 20 m, consistent with the previously noted differences between DOW mast (18 m AGL) and Pod (1 m AGL) observations].

b. Radar measurements of boundary layer and insects. DOW data (Fig. 8, and supplemental animation in the online supplemental material) revealed an early eclipse (1701:38 UTC radar sweep; 33% solar obscuration) ABL characterized by 1–2-km scale HCRs (e.g., Weckwerth et al. 1997) typical of a convective summertime ABL in the High Plains. Doppler velocity fields (in this clear-air context, radars are likely measuring the velocity of airborne/flying insects not true air velocities, as discussed below) indicate motion from approximately north, roughly perpendicular to the path of the eclipse, at ~11–12 m s^{-1} at and above ~100 m AGL. Radar-measured HCR structures weakened substantially by 1725 (solar obscuration 67%) and were absent by 1737 (solar obscuration 86%) (evident in the animation and in the 1745:57 UTC still image), as solar obscuration increased beyond 70%, then reappeared again well after totality (evident in the animation and in the 1847:39 UTC still image), consistent with the general stabilization then redestabilization of the ABL associated with near-ground cooling/warming during the course of the eclipse.[1,2] These observations are consistent with the reduction and reintensification of turbulent motions in the ABL reported by M20.

[1] The apparently longer-wavelength perturbations in the reflectivity and velocity fields, especially visible to the northwest of the radar, are artifacts of azimuthally-varying partial beam blockage in the lowest radar beams. They are anchored to specific azimuths and are not meteorological in origin.

[2] The narrow and elongated region of northward motion in the 1701:38 UTC panel is radar return from a northward moving train (see animation).

Surprisingly, peak Doppler velocities near the surface (50–100 m AGL) increased immediately prior to totality (1745:57 UTC; solar obscuration 99%), the cause of which will be discussed below. Near-ground, ~50 m AGL, peak Doppler velocities decreased substantially by 1746:39 UTC reaching a minimum near 8 m s^{-1} during totality at 1748:29 UTC. Immediately after totality, at 1750:06 UTC (99% obscuration), near-ground peak Doppler velocities had increased to immediate pretotality magnitudes and then dropped again by 1805:48 UTC (76% obscuration). These Doppler velocity variations are quite different from variations in winds observed by the Pods and DOW mast as discussed below.

A roughly north–south radar fine line/kinematic boundary (e.g., Wilson and Schreiber 1986; Boyd 1965), evident as enhanced radar reflectivity and a distinct Doppler wind shift, was observed east of the line of DOWs and propagated approximately westward, roughly perpendicular to the ambient wind direction (1847:33 UTC). This line eventually crossed the DOWs and Pods, around 1940–50, about an hour after the detailed analysis period. The radars had shut down at about 1900, and only two Pods remained deployed to observe the wind shift and wind speed decrease discussed above. The cause of this feature cannot be unambiguously attributed to this eclipse. Boundaries have been associated with heat flux gradients (e.g., Segal and Arritt 1992). Such fine lines are sometimes associated with outflow caused by evaporatively driven cooling related to precipitation; however, no storms had occurred near the study area recently, and the line was not evident before the eclipse. Previous studies have attributed eclipse-associated wind shifts to "cyclones" (Clayton 1901) and to general changes in the ABL (Gray and Harrison 2016).

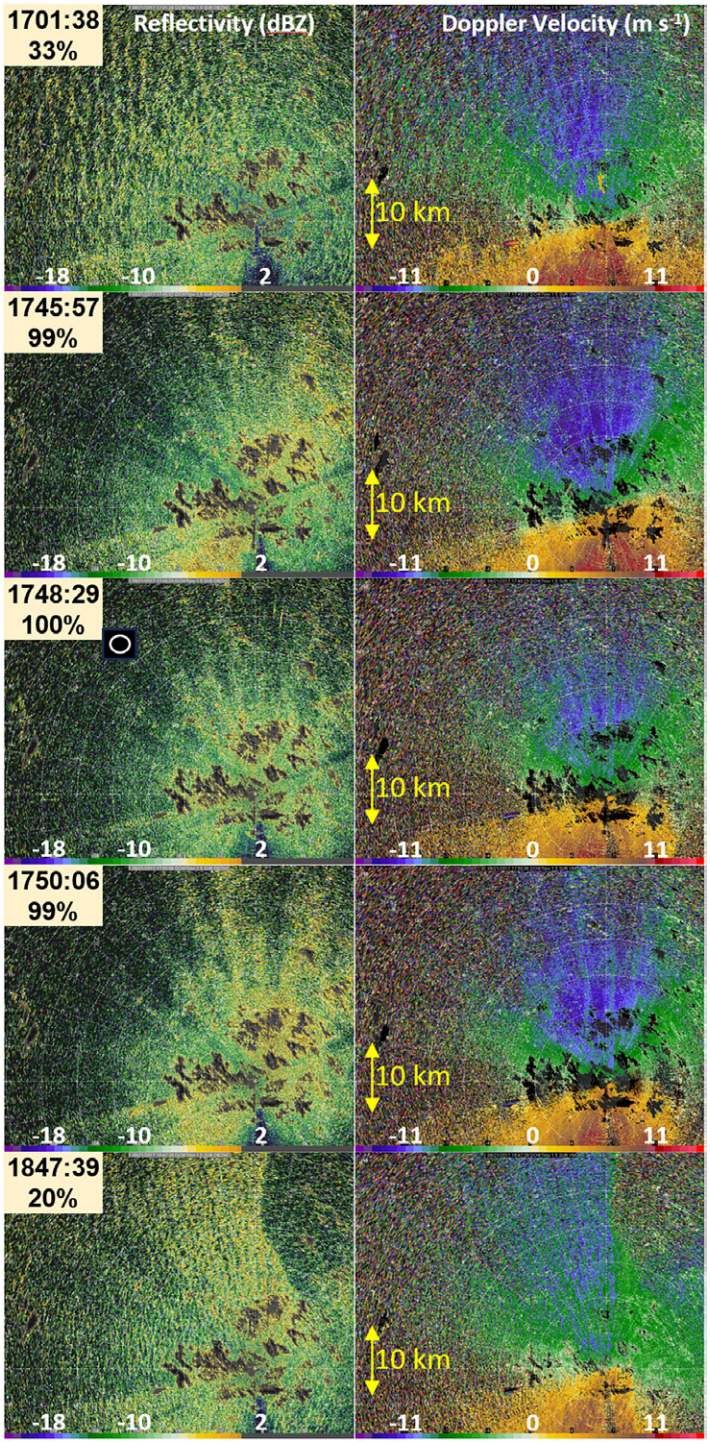

Fig. 8. DOW low-level (0.5°) sweeps during the eclipse. Changes in ABL structure associated with changes in thermodynamic stability, insect behavior, and a wind shift fine line are shown. (left) Uncalibrated radar reflectivity and (right) Doppler velocity. White key text is reflectivity (dBZ) and Doppler velocity (m s^{-1}). Scan times are in HHMM:SS UTC. Range rings are at 5-km intervals. Percent solar obscuration is annotated for each sweep time.

However, in this case, Pod data indicate very little wind direction variation in the 1000 s prior to, during, or after totality, at least in the very small study region (see discussion above and Fig. 5). The current observations show that small-scale boundaries, or other short-duration, discrete phenomena, perhaps usually unobserved, may be the causes of wind changes during the prolonged period of eclipses. It is possible that this fine line was associated with unobserved during- or near-totality wind velocity changes outside the study region. Winds veer somewhat between 1700 and 1800 UTC at both Torrington (TOR), Nebraska, and Scottsbluff (BFF), Nebraska (Fig. 2), so pre-eclipse wind shift boundaries may have been present. It is therefore recommended that caution be used when associating eclipse-related causality to particular wind velocity changes, especially when confounding, nonsolar factors may be present.

Vector velocities (Fig. 9) at about 350 m AGL were calculated using dual-Doppler techniques (see the appendix) to examine possible localized variations in velocities. During near and full totality portions of the eclipse, vector velocities are nearly homogeneous across the domain, exhibiting primarily small, apparently turbulent, variations, consistent with weakened or

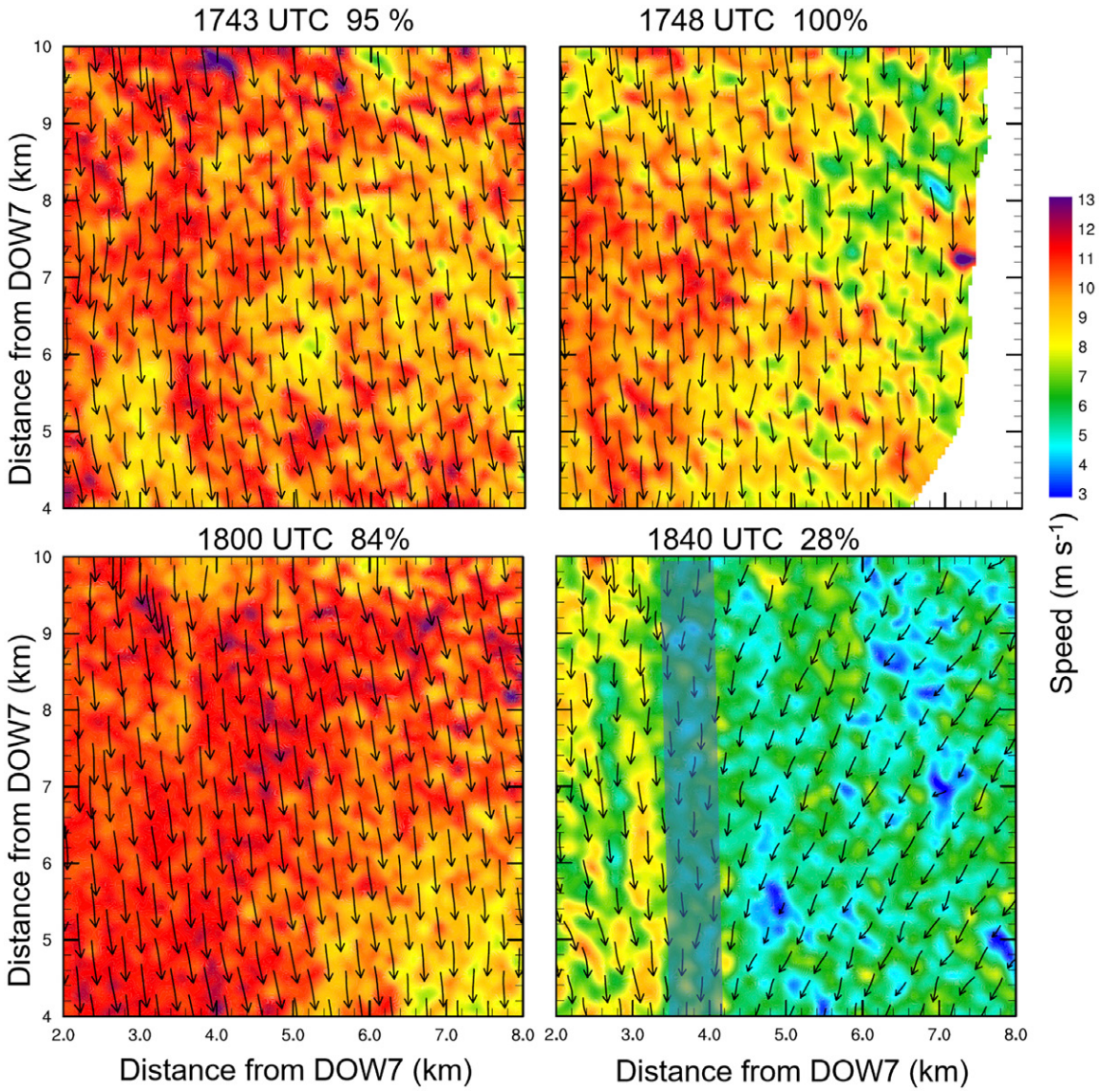

Fig. 9. Dual-Doppler vector and speed fields before, during, and after totality. Horizontal wind vectors (arrows) and speeds (shaded) shortly before (1743 UTC), during (1748 UTC), and shortly after (1800 UTC) totality, and during passage of the radar fine line with wind shift (1840 UTC), annotated schematically with a wide gray line. Percent solar obscuration is annotated for each analysis time.

absent HCRs but also possibly artifacts of poorly resolved scales in the dual-Doppler analysis. Shortly before totality (1743 UTC; 95% obscuration), vector magnitudes were typically 9–12 m s^{-1} from the north; speeds decreased to 8–10 m s^{-1} from nearly due north at totality (1748 UTC), then increased to 10–12 m s^{-1} from the north shortly after (prior to 1800 UTC; 85% obscuration). Well after totality, vectors veered (changed in a clockwise direction) by about 50° and weakened by about 3 m s^{-1} east of the westward-propagating fine line (1840 UTC; 28% obscuration), very consistent with wind velocity changes observed much later when the line crossed some of the Pods and DOW masts around 1940–50.

Variations in Doppler and vector speeds observed by radar (Figs. 8 and 9) very near the time of totality are in contrast to the nearly constant wind speeds directly observed in the balloon soundings (Fig. 7). The rapid drop and recovery in radar-observed speeds are also in contrast to the very gradual drop and lagged recovery observed at the Pods and DOW mast (Figs. 5 and 6). In the nonprecipitating ABL, radars such as DOWs primarily measure the motion of airborne objects, often insects, not the actual winds (Wilson et al. 1994; Russell and Wilson 1996, 1997; Geerts and Miao 2005a,b,c; Martin and Shapiro 2007). Insects and similar "atmospheric plankton" fly at widely varying speeds, with some acting as nearly passive wind field tracers (Zhang et al. 2008), and others flying at substantial speeds relative to the wind (e.g., Knight et al. 2019).

Nonspherical objects such as insects and large raindrops typically exhibit positive differential radar reflectivity (ZDR), the difference between horizontally and vertically polarized radar echo intensity (e.g., Bringi and Chandrasekar 2001; Fabry 2015). Insects, which can be crudely approximated as prolate spheroids, flying/migrating with preferred directionality/major axis oriented in the direction of flight, will present different orientations/profiles relative to radar beams pointed at different angles (e.g., Zhang et al. 2006; Stepanian et al. 2016). For example, insects flying eastward or westward would present end on to an eastward or westward pointing radar beam but would present in full profile to a northward or southward pointing radar beam. Insects observed in full or partial profile will exhibit enhanced ZDR > 0 compared to those observed end on with ZDR ~ 0.

Since the distribution of insect species which were observed by the DOWs is unknown, and different species with different body shapes likely exhibit different ZDRs even when viewed at the same look angle relative to their body orientation, inferences flowing from quantitative comparisons of ZDR patterns are problematic. However, qualitative minima and maxima in ZDR can be employed to assess systematic flight orientations. Early during the eclipse, horizontal reflectivity and ZDR were observed to be maximized toward north-northeast (NNE) (~30° clockwise from north) and SSW (~210°) relative to the DOWs, indicating that the pointing angle of the insects in flight (yaw) was preferentially toward the east-southeast (120°) or west-northwest (300°) (Fig. 10 and supplemental animation).[3] This approximately NNE–south-southwest (SSW) oriented ZDR enhancement disappeared during totality near 1748 UTC, then reappeared afterward, consistent with insects ceasing their preferred east-southeastward orientation during totality, then reestablishing it in a similar direction after.

[3] The ZDR signal is quite noisy, and complicated by ground clutter returns. Objective best fits of the azimuthal dependency ZDR at constant ranges (not shown), and at varying radar scan elevations, and different DOWs, reveal qualitative ZDR peaks from 200° to 240° (SW) and 20°–60° (NE) before and after totality, with nearly no azimuthal dependence at totality.

Azimuthally averaged (median) radar reflectivity, velocity–azimuth display (VAD; Browning and Wexler 1968) analyses, and sounding data are used to further reveal the behavior of the radar-observed insects during the eclipse. Layers of insects in the ABL are evident in the VAD analysis, with the strongest radar echoes at 200–300 m AGL (Fig. 11). While there may be a weak tendency for these layers to descend after 1742 UTC, they remain at essentially the same altitude until immediately after 1745 UTC (98% obscuration). Abruptly, after 1745 UTC, the insect layers drop to near the surface. By the end of totality,

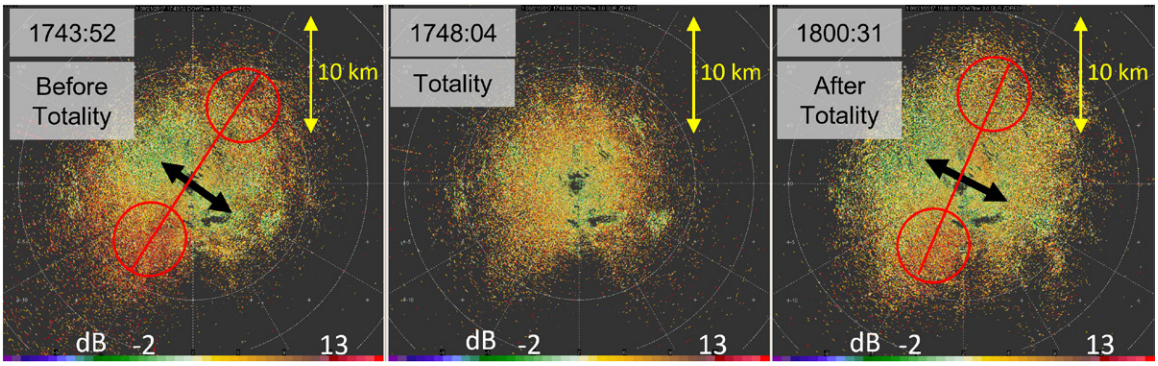

Fig. 10. Insect flight orientation inferred from differential reflectivity (ZDR) before, during, and after totality, revealing insect orientation, as observed by DOW7. (left) Before totality, there are regions of enhanced (brown and red shading, annotated with red ovals) and minimized (green and white shading) ZDR. Qualitative insect orientation directions (black arrows) are inferred from the orientations of the maximum and minimum regions as annotated. (center) During totality, ZDR does not show directional dependence. This combined with reduced reflectivity (Fig. 8) indicates that most insects have landed and that any that remain airborne do not exhibit a preferred flight direction. (right) After totality, the NNE-SSW oriented pattern is reestablished, indicating that insects are resuming approximately their original flight direction. The ZDR is only crudely calibrated, with this analysis focusing on the qualitative orientation of enhancement regions, not quantitative values. Values are in decibels. Times are in HHMM:SS UTC.

at 1749 UTC, radar reflectivity has dropped in intensity by more than half (> 3 dB) near the surface and by nearly 90% (10 dB) at 600 m AGL. Immediately after totality, at 1750 UTC, an intense bloom of insects rises quickly to 200–600 m AGL, with climb rates initially exceeding 1 m s^{-1} for 50–100 s, with climb rates of 0.5 m s^{-1} persisting for ~500 s.

VAD analysis reveals speeds increasing from 9 m s^{-1} at 100 m AGL to 11–13 m s^{-1} above 600 m. But then, abruptly at totality, speeds decline, dropping to 9–10.5 m s^{-1} throughout the 50–1000 m AGL layer immediately after totality. Speed values measured by radar during and immediately after totality are nearly exactly those measured by the purely air–velocity measuring soundings (Fig. 7), indicating that the VAD speed field at and immediately after totality represents purely air velocities, not the motion of airborne insects. This, combined

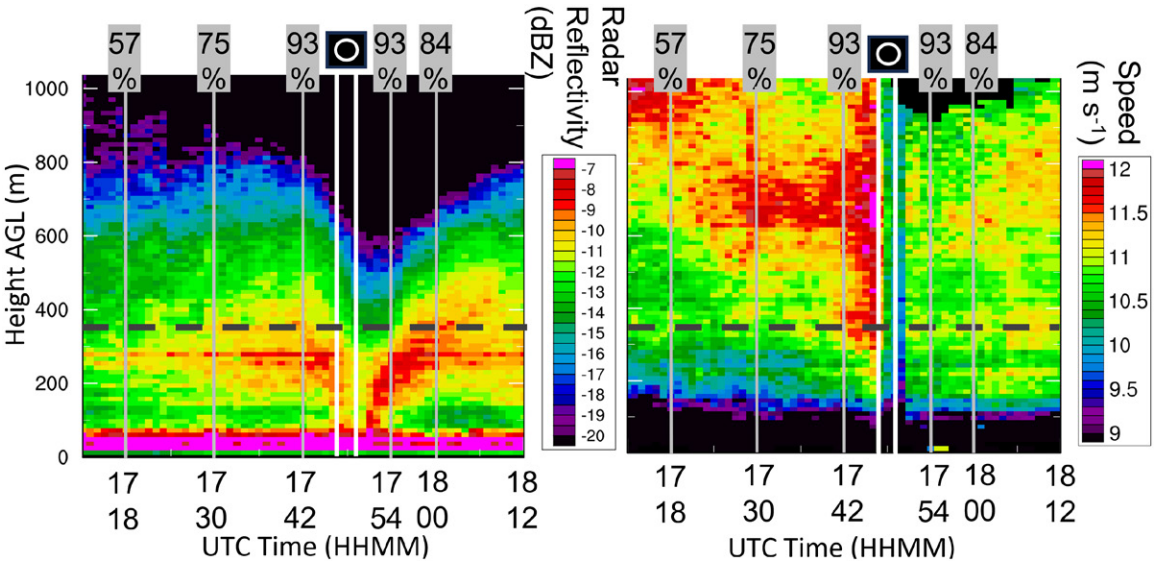

Fig. 11. Vertical cross sections of insect layer evolution during the eclipse. (left) DOW7 azimuthally averaged uncalibrated radar reflectivity showing insects dropping rapidly at totality and then rising; (right) VAD-derived wind speed, showing an abrupt and substantial reduction at totality and the slow recovery after. Horizontal black lines highlight dual-Doppler vector analysis altitude in Fig. 9. Percent solar obscuration is annotated with gray lines and totality with white lines and icon. Times are in HHMM UTC.

with the substantial decreases in radar reflectivity, indicates that nearly all insects land during totality. VAD speeds increase again after totality, exceeding pretotality levels below 400 m AGL (consistent with the dual-Doppler analysis at 350 m AGL at 1800 UTC), but do not fully recover at 500–1000 m AGL. This suggests that, after totality, the higher-flying insects at 500–1000 m are flying at slightly slower horizontal speeds compared to before totality.

Abrupt behavioral changes immediately at totality, such as those documented here, might be expected if insects are using solar "compasses," as described by, e.g., Beetz and Jundi (2018) and Massy et al. (2021). Effects of temperature and boundary layer evolution (e.g., the "collapse" noted by M20) can be excluded. It is well known that air temperature affects insect flight behavior (e.g., Dry and Taylor 1970; Taylor 1963; Saha et al. 2024), but this can be excluded as a causal mechanism in this case since air temperatures are nearly constant, within about 0.2°C, from 100 to 700 m AGL (see Fig. 7). Insects are not just following the collapse of the ABL since the changes in ABL structure are evident ~1000 s or more before totality in this case (as well as in M20), while the rapid lowering of the most reflective insect layers at and near 300 m AGL occurs only after 1745 UTC, less than 200 s before totality, and the decrease in altitude of the higher-flying insects begins slightly earlier, perhaps as early as 1742 UTC, still after 93% total obscuration. The current result is in striking contrast to those of Stepanian and Wainwright (2020), who, critically, used observations from a distance far away (~300 km) from totality, so insects near their observations would never have experienced totality. It is also in contrast to the results reported in the temporally coarse analysis presented in Nilsson et al. (2018). The National Weather Service weather radars producing the data used in their analysis employed volumetric repeat intervals of 300–360 s, which was far longer than the period of totality at any of the sites. Even at the few sites which experienced totality, their results primarily reflect, and are strongly aliased toward, responses to partial solar obscuration. They note in passing at the only five sites with any radar scans during totality (critically, never complete radar volumes), there were "sudden peaks in the numbers of biological targets at low altitudes. . . only during totality," which do not reflect their long-period analysis revealing generally reduced biologic signals "at low levels of obscuration." They do note that their data might indicate insects having a "more immediate and explicit reaction to darkness." We surmise that the current DOW short-temporal-update volumetric analyses explicitly map out the temporal and vertical responses which caused the peaks in insect numbers likely observed in the low-level sweeps noted by Nilsson et al. (2018).

Subtraction of purely air–velocity measuring balloon sounding profiles from insect-velocity measuring radar VAD profiles reveals the air-relative speed ("airspeed") and air-relative flight direction of the insects (Fig. 12). This analysis involves the vector subtraction of two similarly valued velocities, each exhibiting errors of ~1 m s^{-1} magnitude, so the resulting residual, the insect air-relative velocities, is noisy, with precise values suspect.[4] Examination of the results using six VADs, three from each of DOW6 and DOW7, subtracting from cotemporal balloon soundings, reveals that, generally, insects at 100–500 m AGL were flying at about 1 m s^{-1}, while insects at 600–800 m AGL flew at about 2–3 m s^{-1}. These different flight speeds, and differing pre- versus posttotality behavior revealed in the VAD analysis, are consistent with different species flying at different altitudes. Throughout the ABL, insects were, generally, flying toward the east-southeast to Southeast, embedded in, and relative to, the northerly winds,[5] while being carried by these stronger winds in a generally southward direction, consistent with, but with slower airspeed wind-assisted motions described by, e.g., Chapman et al. (2008) of faster-flying nocturnal moths and Knight et al. (2019) for relatively fast-flying diurnally flying insects.

[4] Of the six different insect velocity vertical profiles, there is one speed outlier (using DOW6 1739 UTC VAD) and one direction outlier (using DOW7 1727 UTC VAD), but five out of six show consistency.

[5] By convention, wind directions reflect the origin direction of the air, while flight directions reflect the destination direction of objects.

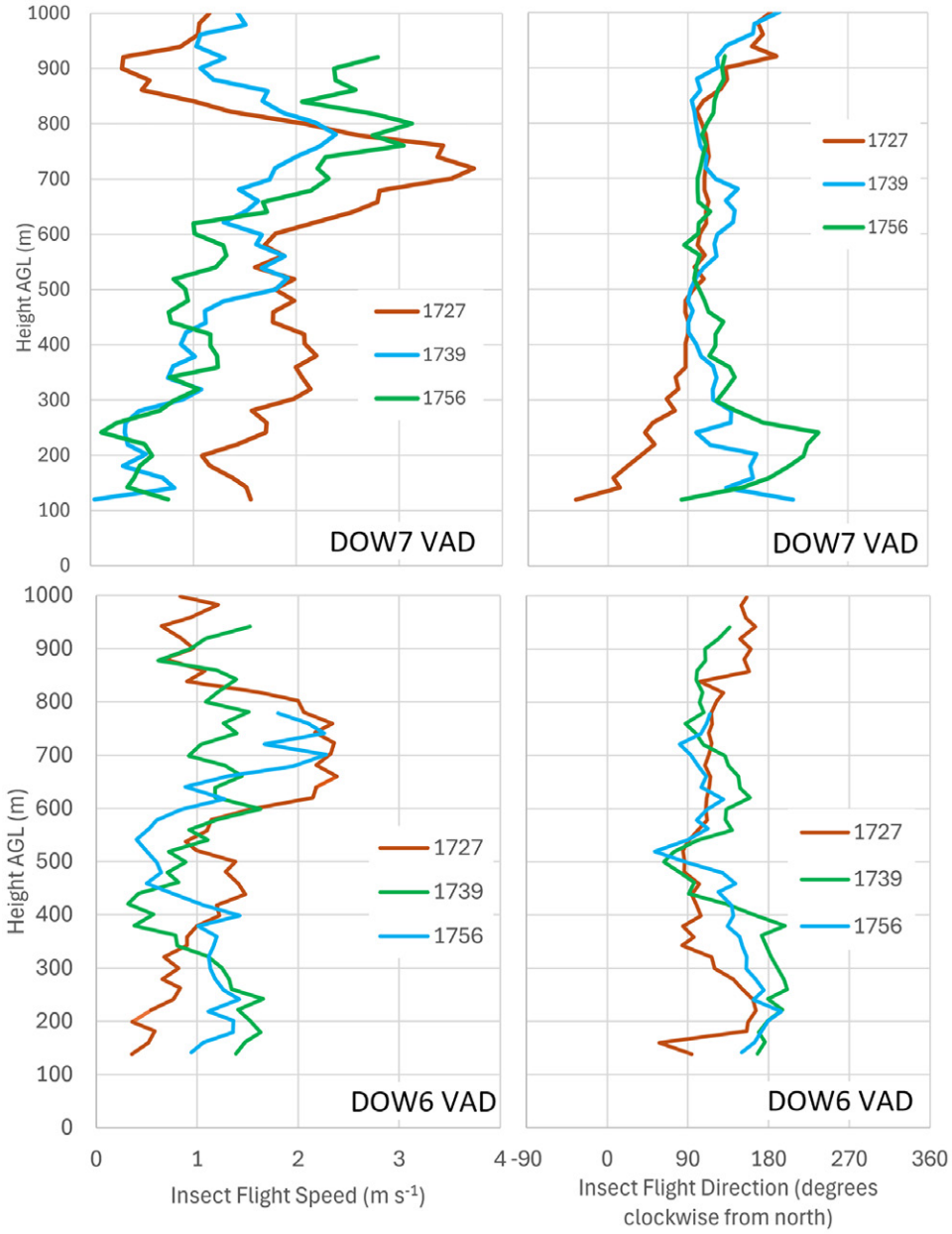

Fig. 12. Vertical cross sections of insect flight velocities before and after totality. (left) Insect flight speed and (right) insect flight direction (clockwise from north) calculated from differences in air (sounding measured) and insect (radar measured) velocities. Times are in HHMM UTC.

The VAD/sounding-deduced air-relative insect flight direction to the Southeast is consistent with the insect pointing direction (yaw) inferred from the ZDR data as discussed above. Flight speeds of 1–2 m s^{-1} are substantially smaller than those documented for some rapidly flying migratory insects (e.g., Knight et al. 2019; Chapman et al. 2008) and more consistent with slowly flying species such as some aphids (Zhang et al. 2008), some ladybirds (Lombaert et al. 2014), and some migratory butterflies (Minter et al. 2018).

5. Summary

Targeted observations from multiple radars, atmospheric soundings, and in situ weather stations in and very near solar eclipse totality were used to deduce ABL and insect behavioral changes. Substantial temperature decreases of 4°–6°C and wind speed decreases of 3 m s^{-1} were observed at surface weather stations experiencing totality. ABL temperatures and wind speeds above 100 m AGL remained nearly constant. Wind direction changes near the surface

and aloft were not observed proximate to totality, but occurred with the passage of a discrete wind shift fine line well after totality. Surface temperature and wind speed oscillations suggest that ABL convective processes, while suppressed, did not dissipate completely. Wind speeds, directions, and potential temperatures were nearly constant above 100 m, indicating that eclipse-caused ABL responses were limited to very near the surface. Airborne insect flight velocities and orientations were deduced by combining proximate radar and balloon sounding velocity data, and dual-polarization data. Insects did not change flight behavior in response to increasing partial phases of the eclipse up to at least 93% obscuration, but dropped abruptly to the ground only during near to 100% totality, quickly rising again and resuming their original flight direction (albeit more slowly) afterward, consistent with the use of "solar compass" navigation. These represent the most detailed and fine-spatial, three-dimensional, and temporal-scale observations of atmospheric and insect responses to eclipse totality.

Acknowledgments. We thank Maiana Hanshaw for editing this manuscript and the crew of the eclipse totality mission including Andrew Frambach, James Marquis, Trevor White, Traeger Meyer, Ling Chan, and Ethan Wurman.

Data availability statement. Data are available at the permanent data repository of the Flexible Array of Radars and Mesonets (FARM), available through FTP, with instructions at the FARM web page (https://www.farmfacility.org/).

APPENDIX
Instrumentation, Data, and Analysis Details

Pods and a DOW-mounted mast collected standard meteorological data at 1 Hz. RM Young 5103 and Gill WindsSonic 75 anemometers and Rotronic HC2S3-L temperature/relative humidity probes were used. Temperature and wind speed data were smoothed using a 21-s mean to reveal long-period trends, except for DOW6 mast temperature data smoothed with a 61-s mean, since it was very noisy due to instrument problems. DOW8 mast temperature data were unsuitable for analysis. Pod wind direction data were smoothed using a 61-s median filter, and then the mean of all the Pod data at each time was calculated. The purpose of this averaging was to discern any small general wind direction change during the eclipse, while individual Pod wind direction time series exhibit considerable second-by-second variations due to short-duration turbulent motions in the atmosphere. Data from Pod H were excluded from the analysis since it became anomalous during the eclipse for unknown reasons, exhibiting lower temperatures and wind speeds. Pod H siting was similar to that of other Pods, and it was not on a rise or depression. It is speculated that a vehicle may have parked nearby during the eclipse, or that an isolated irrigated field may have resulted in anomalous measurements. This exclusion does not substantively alter any of the results or conclusions of this manuscript since Pod averages only are discussed and serves only to clarify the presentation.

Vertical profiles of winds and temperatures were measured by atmospheric soundings using Graw DFM-09 sondes carried aloft by helium balloons. Launch conditions, including initial pressures and winds used the most proximate Pod data. GPS-determined altitudes are used in the current analysis. Data below 40 m AGL are a blend of surface initialization and direct sonde measurements.

DOWs conducted surveillance-type scans at 0.5°–4.0° above the horizon, with intervolume intervals of 50 s. Range sampling and pulse lengths were matched at 50 m. Velocity data from samples exhibiting very low power, below –107 dBm, were filtered. VAD and azimuthally averaged (median) reflectivity analysis were conducted on 4° elevation radar sweeps with a

vertical spacing determined by sin (beam elevation) x gate spacing (50 m), which was about 3.5 m, and ground clutter echoes with <3 m s^{-1} removed.

Two-dimensional horizontal dual-Doppler vector analyses were conducted by resampling DOW6 and DOW8 data from a single tilt, 2°, to a common Cartesian grid with 50-m grid spacing, using a two-pass Barnes analysis (Majcen et al. 2008) with Kappa = 0.014 km^2 and Gamma = 0.3. Standard dual-Doppler techniques were used to calculate horizontal vectors from the Doppler measurements from both radars (e.g., Armijo 1969; Miller and Strauch 1974; Lhermitte and Miller 1970; Kosiba et al. 2013). VAD analyses used the 4° DOW sweeps.

Sounding and VAD analyses were resampled to 20-m vertical spacing so that differences could be calculated and for readability. Data from the 1756 UTC sonde below 141 m AGL are missing since the sonde did not maintain GPS lock for several seconds after launch. Data below 120 m AGL were excluded from the bug velocity analysis since radar data were contaminated by clutter, and sounding wind data were blended with surface anemometer wind data in this layer.

The evolution of the radar reflectivity and Doppler velocity fields, revealing changes in HCRs, the propagation of the fine line, and responses of insects discussed in the main text, is illustrated with animations of radar imagery provided in the supplemental material. The presence, then disappearance, of HCR, the contracting then expanding ring of enhanced radar reflectivity maximized to the NNE and SSW, and the approach of the radar fine line from the east are evident.

References

Aplin, K. L., C. J. Scott, and S. L. Gray, 2016: Atmospheric changes from solar eclipses. *Philos. Trans. Roy. Soc.*, **A374**, 20150217, https://doi.org/10.1098/rsta.2015.0217.

Armijo, L., 1969: A theory for the determination of wind and precipitation velocities with Doppler radars. *J. Atmos. Sci.*, **26**, 570–573, https://doi.org/10.1175/1520-0469(1969)026<0570:ATFTDO>2.0.CO;2.

Armitage, P., and R. Doll, 1954: The age distribution of cancer and a multi-stage theory of carcinogenesis. *Br. J. Cancer*, **8**, 1–12, https://doi.org/10.1038/bjc.1954.1.

Beetz, M. J., and B. E. Jundi, 2018: Insect orientation: Stay on course with the sun. *Curr. Biol.*, **28**, R933–R936, https://doi.org/10.1016/j.cub.2018.07.032.

Boyd, J. G., 1965: Weather note: Observation of two intersecting radar fine lines. *Mon. Wea. Rev.*, **93**, 188, https://doi.org/10.1175/1520-0493(1965)093<0188:OOTIRF>2.3.CO;2.

Bringi, V. N., and V. Chandrasekar, 2001: *Polarimetric Doppler Weather Radar: Principles and Applications.* Cambridge University Press, 636 pp.

Browning, K. A., and R. Wexler, 1968: The determination of kinematic properties of a wind field using Doppler radar. *J. Appl. Meteor.*, **7**, 105–113, https://doi.org/10.1175/1520-0450(1968)007<0105:TDOKPO>2.0.CO;2.

Buban, M. S., T. R. Lee, E. J. Dumas, C. B. Baker, and M. Heuer, 2019: Observations and numerical simulation of the effects of the 21 August 2017 North American total solar eclipse on surface conditions and atmospheric boundary-layer evolution. *Bound.-Layer Meteor.*, **171**, 257–270, https://doi.org/10.1007/s10546-018-00421-4.

Chapman, J. W., D. R. Reynolds, H. Mouritsen, J. K. Hill, J. R. Riley, D. Sivell, A. D. Smith, and I. P. Woiwod, 2008: Wind selection and drift compensation optimize migratory pathways in a high-flying moth. *Curr. Biol.*, **18**, 514–518, https://doi.org/10.1016/j.cub.2008.02.080.

Clark, M. R., 2016: On the variability of near-surface screen temperature anomalies in the 20 March 2015 solar eclipse. *Philos. Trans. Roy. Soc.*, **A374**, 20150213, https://doi.org/10.1098/rsta.2015.0213.

Clayton, H. H., 1901: Clayton's eclipse cyclone and the diurnal cyclones. *Science*, **13**, 747–750, https://doi.org/10.1126/science.13.332.747.

Dry, W. W., and L. R. Taylor, 1970: Light and temperature thresholds for take-off by aphids. *J. Anim. Ecol.*, **39**, 493–504, https://doi.org/10.2307/2984.

Fabry, F., 2015: *Radar Meteorology: Principles and Practice.* Cambridge University Press, 256 pp.

French, J. R., and Coauthors, 2018: Precipitation formation from orographic cloud seeding. *Proc. Natl. Acad. Sci. USA*, **115**, 1168–1173, https://doi.org/10.1073/pnas.1716995115.

Geerts, B., and Q. Miao, 2005a: A simple numerical model of the flight behavior of small insects in the atmospheric convective boundary layer. *Environ. Entomol.*, **34**, 353–360, https://doi.org/10.1603/0046-225X-34.2.353.

——, and ——, 2005b: Airborne radar observations of the flight behavior of small insects in the atmospheric convective boundary layer. *Environ. Entomol.*, **34**, 361–377, https://doi.org/10.1603/0046-225X-34.2.361.

——, and ——, 2005c: The use of millimeter Doppler radar echoes to estimate vertical air velocities in the fair-weather convective boundary layer. *J. Atmos. Oceanic Technol.*, **22**, 225–246, https://doi.org/10.1175/JTECH1699.1.

——, and Coauthors, 2017: The 2015 Plains Elevated Convection at Night Field project. *Bull. Amer. Meteor. Soc.*, **98**, 767–786, https://doi.org/10.1175/BAMS-D-15-00257.1.

Gray, S. L., and R. G. Harrison, 2016: Eclipse-induced wind changes over the British Isles on the 20 March 2015. *Philos. Trans. Roy. Soc.*, **A374**, 20150224, https://doi.org/10.1098/rsta.2015.0224.

Hanna, E., and Coauthors, 2016: Meteorological effects of the solar eclipse of 20 March 2015: Analysis of UK Met Office automatic weather station data and comparison with automatic weather station data from the Faroes and Iceland. *Philos. Trans. Roy. Soc.*, **A374**, 20150212, https://doi.org/10.1098/rsta.2015.0212.

Knight, S. M., G. M. Pitman, D. T. T. Flockhart, and D. R. Norris, 2019: Radio-tracking reveals how wind and temperature influence the pace of daytime insect migration. *Biol. Lett.*, **15**, 20190327, https://doi.org/10.1098/rsbl.2019.0327.

Kosiba, K. A., and J. Wurman, 2014: Finescale dual-Doppler analysis of hurricane boundary layer structures in Hurricane Frances (2004) at landfall. *Mon. Wea. Rev.*, **142**, 1874–1891, https://doi.org/10.1175/MWR-D-13-00178.1.

——, ——, Y. Richardson, P. Markowski, P. Robinson, and J. Marquis, 2013: Genesis of the Goshen County, Wyoming, Tornado on 5 June 2009 during VORTEX2. *Mon. Wea. Rev.*, **141**, 1157–1181, https://doi.org/10.1175/MWR-D-12-00056.1.

——, ——, K. Knupp, K. Pennington, and P. Robinson, 2019: Ontario Winter Lake-effect Systems (OWLeS): Bulk characteristics and kinematic evolution of misovortices in long-lake-axis-parallel snowbands. *Mon. Wea. Rev.*, **148**, 131–157, https://doi.org/10.1175/MWR-D-19-0182.1.

——, and Coauthors, 2024: The Propagation, Evolution, and Rotation in Linear Storms (PERiLS) project. *Bull. Amer. Meteor. Soc.*, **105**, E1768–E1799, https://doi.org/10.1175/BAMS-D-22-0064.1.

Lachenmeier, E., and Coauthors, 2024: Irrigated agriculture significantly modifies seasonal boundary layer atmosphere and lower-tropospheric convective environment. *J. Appl. Meteor. Climatol.*, **63**, 245–262, https://doi.org/10.1175/JAMC-D-23-0020.1.

Lhermitte, R. M., and L. J. Miller, 1970: Doppler radar methodology for the observation of convective storms. *14th Radar Meteorology Conf.*, Tucson, AZ, Amer. Meteor. Soc., 133–138.

Lombaert, E., A. Estoup, B. Facon, B. Joubard, J.-C. Grégoire, A. Jannin, A. Blin, and T. Guillemaud, 2014: Rapid increase in dispersal during range expansion in the invasive ladybird *Harmonia axyridis*. *J. Evol. Biol.*, **27**, 508–517, https://doi.org/10.1111/jeb.12316.

Mahmood, R., and Coauthors, 2020: The Total Solar Eclipse of 2017: Meteorological observations from a statewide mesonet and atmospheric profiling systems. *Bull. Amer. Meteor. Soc.*, **101**, E720–E737, https://doi.org/10.1175/BAMS-D-19-0051.1.

Majcen, M., P. Markowski, Y. Richardson, D. Dowell, and J. Wurman, 2008: Multipass objective analysis of Doppler radar data. *J. Atmos. Oceanic Technol.*, **25**, 1845–1858, https://doi.org/10.1175/2008JTECHA1089.1.

Marquis, J. N., Y. P. Richardson, and J. M. Wurman, 2007: Kinematic observations of misocyclones along boundaries during IHOP. *Mon. Wea. Rev.*, **135**, 1749–1768, https://doi.org/10.1175/MWR3367.1.

Martin, W. J., and A. Shapiro, 2007: Discrimination of Bird and insect radar echoes in clear air using high-resolution radars. *J. Atmos. Oceanic Technol.*, **24**, 1215–1230, https://doi.org/10.1175/JTECH2038.1.

Massy, R., W. L. S. Hawkes, T. Doyle, J. Troscianko, M. H. M. Menz, N. W. Roberts, J. W. Chapman, and K. R. Wotton, 2021: Hoverflies use a time-compensated sun compass to orientate during autumn migration. *Proc. Biol. Sci.*, **288**, 20211805, https://doi.org/10.1098/rspb.2021.1805.

Miller, L. J., and R. G. Strauch, 1974: A dual Doppler radar method for the determination of wind velocities within precipitating weather systems. *Remote Sens. Environ.*, **3**, 219–235, https://doi.org/10.1016/0034-4257(74)90044-3.

Minter, M., A. Pearson, K. S. Lim, K. Wilson, J. W. Chapman, and C. M. Jones, 2018: The tethered flight technique as a tool for studying life-history strategies associated with migration in insects. *Ecol. Entomol.*, **43**, 397–411, https://doi.org/10.1111/een.12521.

NASA, 2024: Solar eclipse website. https://eclipse.gsfc.nasa.gov/solar.html.

Nilsson, C., K. G. Horton, A. M. Dokter, B. M. Van Doren, and A. Farnsworth, 2018: Aeroecology of a solar eclipse. *Biol. Lett.*, **14**, 20180485, https://doi.org/10.1098/rsbl.2018.0485.

Rabin, R. M., and R. J. Doviak, 1989: Meteorological and astronomical influences on radar reflectivity in the convective boundary layer. *J. Appl. Meteor.*, **28**, 1226–1235, https://doi.org/10.1175/1520-0450(1989)028<1226:MAAIOR>2.0.CO;2.

Rappin, E., and Coauthors, 2021: The Great Plains Irrigation Experiment (GRAINEX). *Bull. Amer. Meteor. Soc.*, **102**, E1756–E1785, https://doi.org/10.1175/BAMS-D-20-0041.1.

Russell, R. W., and J. W. Wilson, 1996: Aerial plankton detected by radar. *Nature*, **381**, 200–201, https://doi.org/10.1038/381200a0.

——, and ——, 1997: Radar-observed "fine lines" in the optically clear boundary layer: Reflectivity contributions from aerial plankton and its predators. *Bound.-Layer Meteor.*, **82**, 235–262, https://doi.org/10.1023/A:1000237431851.

Saha, T., A. P. Genoud, J. H. Park, and B. P. Thomas, 2024: Temperature dependency of insect's wingbeat frequencies: An empirical approach to temperature correction. *Insects*, **15**, 342, https://doi.org/10.3390/insects15050342.

Sanders, F., and J. R. Gyakum, 1980: Synoptic-dynamic climatology of the "Bomb". *Mon. Wea. Rev.*, **108**, 1589–1606, https://doi.org/10.1175/1520-0493(1980)108<1589:SDCOT>2.0.CO;2.

Segal, M., and R. W. Arritt, 1992: Nonclassical mesoscale circulations caused by surface sensible heat-flux gradients. *Bull. Amer. Meteor. Soc.*, **73**, 1593–1604, https://doi.org/10.1175/1520-0477(1992)073<1593:NMCCBS>2.0.CO;2.

Shaffer, T. L., and D. H. Johnson, 2008: Ways of learning: Observational studies versus experiments. *J. Wildl. Manage.*, **72**, 4–13, https://doi.org/https://doi.org/10.2193/2007-293.

Steiger, S. M., and Coauthors, 2013: Circulations, bounded weak echo regions, and horizontal vortices observed within long-lake-axis-parallel–lake-effect storms by the Doppler on wheels. *Mon. Wea. Rev.*, **141**, 2821–2840, https://doi.org/10.1175/MWR-D-12-00226.1.

Stepanian, P. M., and C. E. Wainwright, 2020: Coupling atmospheric and biological remote sensing to investigate boundary-layer evolution and animal flight behavior as affected by the 2017 North American solar eclipse. *Remote Sens.*, **12**, 591, https://doi.org/10.3390/rs12040591.

——, K. G. Horton, V. M. Melnikov, D. S. Zrnic, and S. A. Gauthereaux Jr., 2016: Dual-polarization radar products for biological applications. *Ecosphere*, **7**, e01539, https://doi.org/10.1002/ecs2.1539.

Stull, R. B., 1988: *An Introduction to Boundary Layer Meteorology*. Kluwer Academic Publishers, 666 pp.

Taylor, L. R., 1963: Analysis of the effect of temperature on insects in flight. *J. Anim. Ecol.*, **32**, 99–117, https://doi.org/10.2307/2520.

Weckwerth, T. M., J. W. Wilson, R. M. Wakimoto, and N. A. Crook, 1997: Horizontal convective rolls: Determining the environmental conditions supporting their existence and characteristics. *Mon. Wea. Rev.*, **125**, 505–526, https://doi.org/10.1175/1520-0493(1997)125<0505:HCRDTE>2.0.CO;2.

——, T. W. Horst, and J. W. Wilson, 1999: An observational study of the evolution of horizontal convective rolls. *Mon. Wea. Rev.*, **127**, 2160–2179, https://doi.org/10.1175/1520-0493(1999)127<2160:AOSOTE>2.0.CO;2.

——, and Coauthors, 2004: An overview of the International H2O Project (IHOP_2002) and some preliminary highlights. *Bull. Amer. Meteor. Soc.*, **85**, 253–278, https://doi.org/10.1175/BAMS-85-2-253.

Wilson, J. W., and W. E. Schreiber, 1986: Initiation of convective storms at radar-observed boundary-layer convergence lines. *Mon. Wea. Rev.*, **114**, 2516–2536, https://doi.org/10.1175/1520-0493(1986)114<2516:IOCSAR>2.0.CO;2.

——, T. M. Weckwerth, J. Vivekanandan, R. M. Wakimoto, and R. W. Russell, 1994: Boundary layer clear-air radar echoes: Origin of echoes and accuracy of derived winds. *J. Atmos. Oceanic Technol.*, **11**, 1184–1206, https://doi.org/10.1175/1520-0426(1994)011<1184:BLCARE>2.0.CO;2.

Wurman, J., and J. Winslow, 1998: Intense sub-kilometer-scale boundary layer rolls observed in Hurricane Fran. *Science*, **280**, 555–557, https://doi.org/10.1126/science.280.5363.555.

——, and S. Weygandt, 2003: Mobile radar observations of the Big Elk (2002) and Roberts (2003) fires. *Fifth Symp. on Fire and Forest Meteorology*, Orlando, FL, Amer. Meteor. Soc., J2.10, https://ams.confex.com/ams/FIRE2003/techprogram/paper_65727.htm.

——, and K. Kosiba, 2013: Finescale radar observations of tornado and mesocyclone structures. *Wea. Forecasting*, **28**, 1157–1174, https://doi.org/10.1175/WAF-D-12-00127.1.

——, and ——, 2018: The role of small-scale vortices in enhancing surface winds and damage in Hurricane Harvey (2017). *Mon. Wea. Rev.*, **146**, 713–722, https://doi.org/10.1175/MWR-D-17-0327.1.

——, J. M. Straka, and E. N. Rasmussen, 1996: Fine-scale Doppler radar observations of tornadoes. *Science*, **272**, 1774–1777, https://doi.org/10.1126/science.272.5269.1774.

——, D. Dowel, Y. Richardson, P. Markowski, E. Rasmussen, D. Burgess, L. Wicker, and H. B. Bluestein, 2012: The second verification of the origins of rotation in tornadoes experiment: VORTEX2. *Bull. Amer. Meteor. Soc.*, **93**, 1147–1170, https://doi.org/10.1175/BAMS-D-11-00010.1.

——, K. Kosiba, T. White, and P. Robinson, 2021a: Supercell tornadoes are much stronger and wider than damage-based ratings indicate. *Proc. Natl. Acad. Sci. USA*, **118**, e2021535118, https://doi.org/10.1073/pnas.2021535118.

——, and Coauthors, 2021b: The Flexible Array of Radars and Mesonets (FARM). *Bull. Amer. Meteor. Soc.*, **102**, E1499–E1525, https://doi.org/10.1175/BAMS-D-20-0285.1.

Zhang, P., A., Ryzhkov, and D. Zrnić, 2006: Polarimetric prototype of the WSR-88D radar observations of birds and insect. *12th Conf. on Aviation Range and Aerospace Meteorology*, Atlanta, GA, Amer. Meteor. Soc., P6.4, https://ams.confex.com/ams/Annual2006/webprogram/Paper103618.html.

Zhang, Y., L. Wang, K. Wu, K. A. G. Wyckhuys, and G. E. Heimpel, 2008: Flight performance of the Soybean Aphid, *Aphis glycines* (Hemiptera: Aphididae) under different temperature and humidity regimens. *Environ. Entomol.*, **37**, 301–306, https://doi.org/10.1093/ee/37.2.301.